Electronic Supplementary Material (ESI) for Nanoscale.
This journal is © The Royal Society of Chemistry 2022

Supporting Information

Synthesizing ordered mesoporous Ni spheres with uniform and adjustable size through a one-step Pd^{2+}-assisted soft-templating strategy

Jing Dong,[a] Xueqin Mi,[a] Tingting Sun,*[b] Yixin Zhang,[a] Wenqian Jiang,[a] Fulin Li,[a] Jianfeng Chen[a] and Lianbin Xu*[a]

[a]State Key Laboratory of Organic–Inorganic Composites, Beijing University of Chemical Technology, Beijing 100029, China

[b]Beijing Key Laboratory for Science and Application of Functional Molecular and Crystalline Materials, School of Chemistry and Biological Engineering, University of Science and Technology Beijing, Beijing 100083, China

---

* Corresponding authors. E-mails: xulb@mail.buct.edu.cn (L. Xu); ttsun99@ustb.edu.cn (T. Sun).

Contents

1. Experimental Section

Materials: Nonionic surfactant Brij 58 ($C_{16}H_{33}(OCH_2CH_2)_{20}OH$), Dimethylamine borane (DMAB, $(CH_3)_2NHBH_3$, 97%) and Nafion solution (5 wt%) were purchased from Sigma-Aldrich Co. Nickel (II) chloride hexahydrate ($NiCl_2 \cdot 6H_2O$, 98%) and palladium (II) chloride ($PdCl_2$, 59-60%) were supplied from Aladdin Chemistry Co. Hydrochloric acid (HCl, 36-38%), potassium hydroxide (KOH, 98%) and ethanol (99.7%) were provided from Beijing Chemical Works. All chemicals were used as received without further purification.

Synthesis of OMNiS-x samples. The OMNiS-x samples with uniform and tunable sphere diameter were prepared through a one-step Pd^{2+}-assisted soft-templating strategy by using lyotropic liquid crystals (LLCs) as meso-structural template and Pd nuclei obtained from the reduction of Pd^{2+} ions were used as nucleation sites for directing Ni deposition. To make a templating precursor, 1.0 g Brij 58 was added to a solution containing 2.5 mmol of $NiCl_2$, 28 μmol, 14 μmol, 2.8 μmol, 0.28 μmol and 0.056 μmol of $PdCl_2$, and 0.55 g of HCl solution (1.0×10^{-2} M), obtaining a Brij 58 concentration of 55 wt% (Brij 58/(water + Brij 58)). A closed container was used to avoid evaporation of the water. The obtained mixture was heated to 80 °C under stirring and then cooled down to room temperature. To obtain a homogeneous mixture, the heating and cooling processes were repeated for three times. After cooling to room temperature, the LLCs containing Pd^{2+} and Ni^{2+} were formed. Then, the reducing agent DMAB (~ 0.2 g) was added into the closed vial to reduce Pd^{2+} and Ni^{2+}

ions. The vial was then placed in a water bath that was preheated to 15 °C and kept at 15 °C for 6 hours until the color of the composite completely changed from green to black. After that, the black composite undergoes the washing treatment with ethanol for 5 times to remove the excess reducing agent and surfactant, thus yielding the final OMNiS-50, OMNiS-70, OMNiS-100, OMNiS-140, OMNiS-190 products with average diameter of 50 nm, 70 nm, 100 nm, 140 nm, 190 nm, respectively.

Synthesis of Ni nanoparticles (NiNPs). For comparative studies, The NiNPs without ordered mesostructure was also synthesized. To prepare the solution used for Ni nanoparticle deposition, 2.5 mmol $NiCl_2$ and 2.8 μmol of $PdCl_2$ were dissolved in 1.55 g of HCl (1.0×10^{-2} M) solution. The chemical reduction of Ni^{2+} and Pd^{2+} were performed by adding 0.2 g DMAB to the precursor solution, followed by reaction at 15 °C for 6 hours. The resulting precipitate was centrifuged, washed with ethanol, and then dried at 25 °C in a vacuum overnight to obtain NiNPs.

Synthesis of PMNiS. The comparative sample PMNiS was synthesized through the same fabrication process as that for the OMNiS-x but without adding $PdCl_2$ in the precursor.

Materials Characterization

Scanning electron microscopy (SEM) images were obtained from a Hitachi S-4700 FEG scanning electron microscope. Transmission electron microscopy (TEM), high-resolution TEM (HR-TEM) and selected-area electron diffraction (SAED) images were taken on a JEOL JEM-3010 transmission electron microscope using an accelerating voltage of 200 kV. High-angle annular dark-field scanning transmission electron microscopy (HAADF-STEM) and energy dispersive X-ray spectroscopy (EDS) were performed on a FEI Talos F200X with electron acceleration energy of 200 kV. The Ni and Pd contents in the OMNiS-100 samples were determined by inductively coupled plasma-atomic emission spectrometry (ICP-AES, IRIS Intrepid II XSP, Thermo Elemental). Powder XRD patterns in the range of high diffraction angles were measured by a Rigaku D/max 2500 VB2+/PC diffractometer with monochromatized Cu Kα radiation, while that in the range of low diffraction angles was recorded by a Brucker D8 ADVANCE diffractometer with Co Kα radiation. Nitrogen adsorption-desorption isotherms were measured by using a Micromeritics ASAP 2010 apparatus at 77 K with prior degassing at 100 °C for 6 h. The specific surface areas and average pore sizes were calculated by the BET method and BJH method using the adsorption branches, respectively. X-ray photoelectron spectroscopic (XPS) measurement was carried out on an ESCALAB 250 X-ray photoelectron spectrometer with a monochromatic Al-Kα radiation source.

Electrochemical Characterization

The electrochemical experiments were carried out in a potentiostat/galvanostat (Reference 600, Gamry Instruments) using a conventional three-electrode cell containing a catalyst-coated glassy carbon (GC) rotating disk electrode (5 mm in diameter) as the working electrode, a double junction Ag/AgCl (saturated KCl) electrode as the reference electrode, and a Pt foil as the counter electrode. All potentials measured were quoted against the reversible hydrogen electrode (RHE) using the Nernst equation: $E_{\mathrm{RHE}} = E_{\mathrm{Ag/AgCl}} + 0.059$

pH + 0.197. The working electrode was prepared as follows. 5 mg of catalyst and 45 μl of Nafion solution (5 wt%) was dispersed in 1 ml ethanol by at least 30 min sonication to form a homogeneous ink. Next, 8 μL of the catalyst ink was deposited onto the pre-polished GC electrode with a catalyst loading of ~ 0.2 mg cm^{-2} and then dried in air. Prior to the electrochemical measurement, the electrolyte (0.1 M KOH) in a four-neck round bottom flask was saturated with oxygen to ensure the H_2O/O_2 equilibrium at 1.23 V vs. RHE. Linear sweep voltammograms (LSVs) and cyclic voltammograms (CVs) were acquired at a scan rate of 5 mV s^{-1}, using an electrode rotation speed of 1600 rpm. Electrochemical impedance spectroscopy (EIS) was performed at 1.65 V vs. RHE in the frequency range of 100 kHz to 1 Hz, using a 5 mV amplitude of the sinusoidal voltage. The chronoamperometry measurement was carried out at a constant potential of 1.65 V vs. RHE. The accelerated degradation studies were carried out by cycling the electrode 1000 times and recording the LSV curve after every 100 CV sweeps; each cycle started at 1.0 V and ended at 1.9 V vs. RHE with a scan rate of 100 mV s^{-1} and a rotational speed of 1600 rpm. All electrochemical data were corrected for 90% ohmic potential drop (iR) using the uncompensated ohmic electrolyte resistance R. The R was determined to be ~ 42 Ω in 0.1 M KOH electrolyte by high-frequency impedance method at the potential of 1.0 V vs. RHE, and iR compensation was applied using the electrochemical analyzer software during the measurements.

Calculation methods:

The overpotential (η) was calculated according to the following equation:

$$\eta = E \text{ (vs. RHE)} - 1.23 \qquad \text{(S1)}$$

The values of mass activity (A g^{-1}) were calculated from the catalyst loading m (0.2 mg cm_{geo}^{-2}) and the measured current density J (mA cm_{geo}^{-2}) at the potential of 1.6 V vs. RHE:

$$\text{mass activity} = \frac{J}{m} \qquad \text{(S2)}$$

The values of specific activity (mA cm^{-2}) were calculated from the BET surface area S_{BET} (m^2 g^{-1}), catalyst loading m (0.2 mg cm_{geo}^{-2}), and the measured current density J (mA cm_{geo}^{-2}) at the potential of 1.6 V vs. RHE:

$$\text{specific activity} = \frac{J}{10 \cdot \text{SBET} \cdot m} \qquad \text{(S3)}$$

The values of TOF were calculated by assuming that every metal atom is involved in the catalysis (lower TOF limits were calculated):

$$\text{TOF} = \frac{J \cdot \text{Sgeo}}{4\,F \cdot n} \qquad \text{(S4)}$$

Here, J (mA cm_{geo}^{-2}) is the measured current density at the potential of 1.6 V vs. RHE, S_{geo} (0.196 cm^2) is the surface area of glassy carbon disk, the number 4 means 4 electrons per mole of O_2, F is the Faraday's constant (96485.3 C mol^{-1}), and n is the moles of the metal atom on the electrode calculated from m and the molecular weight of the coated catalysts.

The calculation of electrochemically active surface area (ECSA) is based on the measured double layer capacitance of the studied electrode according to previously published reports.[1,2] To measure double-layer charging via CV, a potential range in which no apparent Faradaic processes occur was determined from static CV. The charging current i_c was measured from the CVs at different scan rates. The relation between i_c, the scan rate (v) and the double layer capacitance (C_{DL}) was given in equation S5.

$$i_c = vC_{DL} \qquad \text{(S5)}$$

Therefore, the slope of i_c as a function of v will give a straight line with the slope equal to C_{DL}. The ECSA is calculated from the double layer capacitance according to equation S6:

$$\text{ECSA} = \frac{C_{DL}}{C_s} \qquad \text{(S6)}$$

where C_s is the specific capacitance of the catalyst. And a general specific capacitance of $C_s = 0.040$ mF cm^{-2} is accepted based on typical reported values.[2]

2. Supplementary Figures

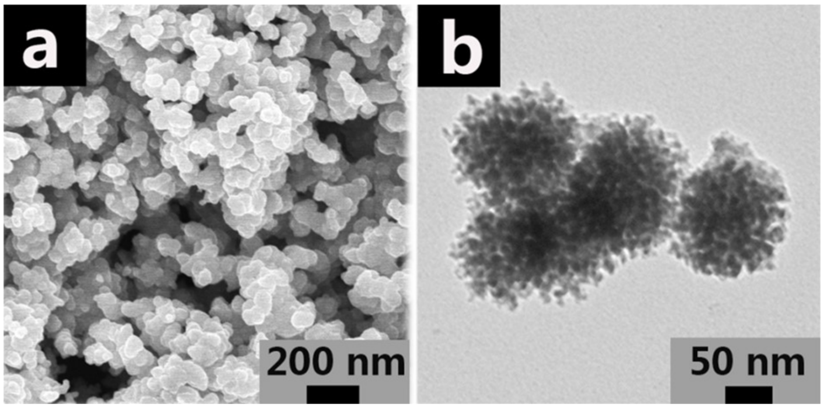

Fig. S1 (a) SEM and (b) TEM image of NiNPs.

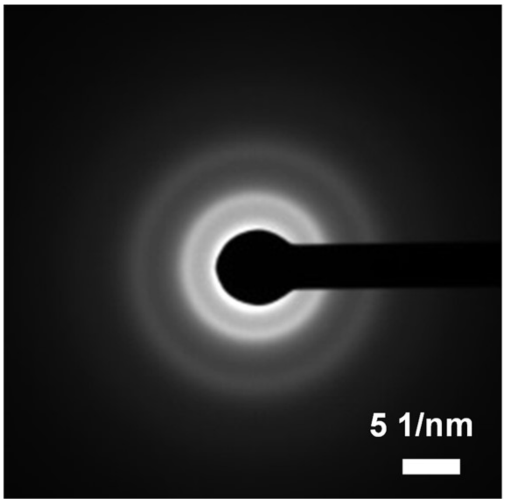

Fig. S2 Selected-area electron diffraction (SAED) image of the OMNiS-50 sample.

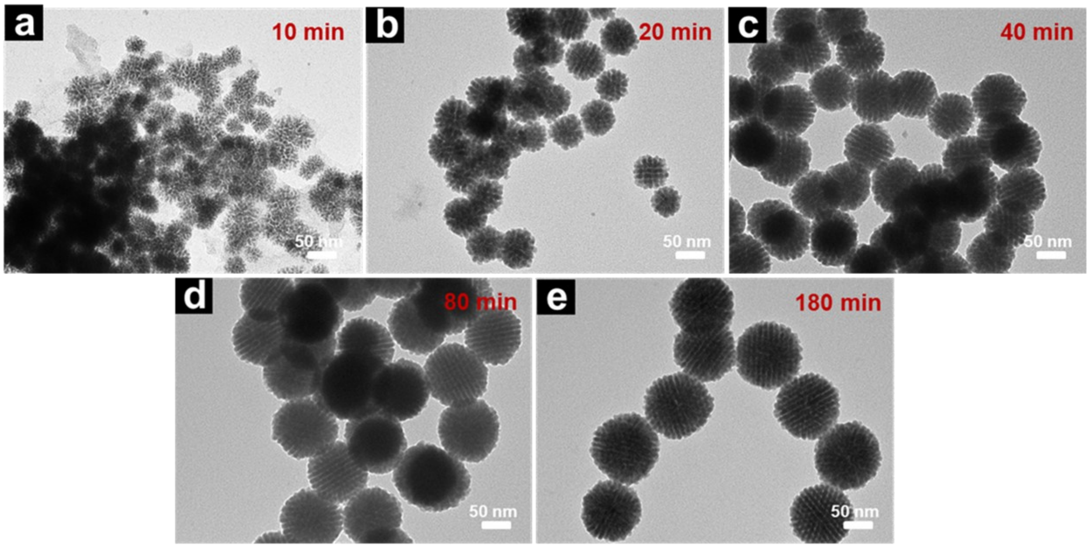

Fig. S3 TEM images of the OMNiS-100 sample taken at different reaction times: (a) 10 min, (b) 20 min, (c) 40 min, (d) 80 min, (e) 180 min.

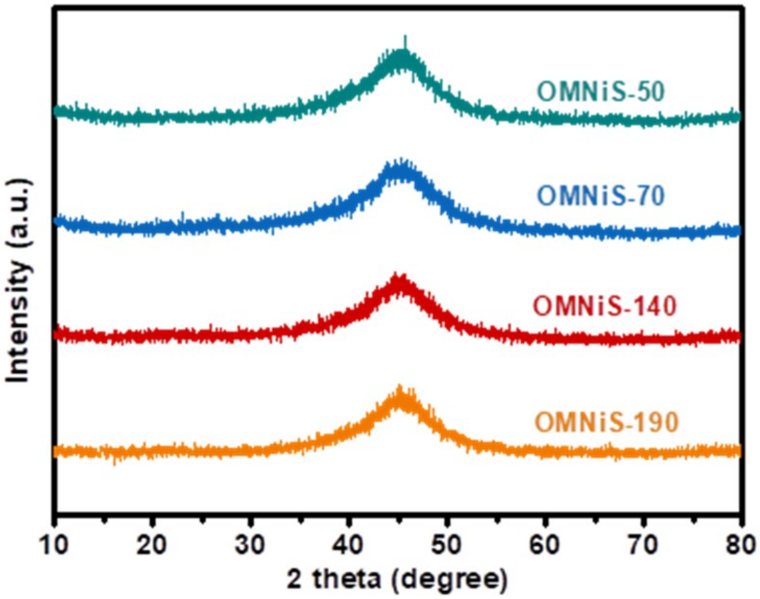

Fig. S4 Wide-angle XRD patterns of the OMNiS samples.

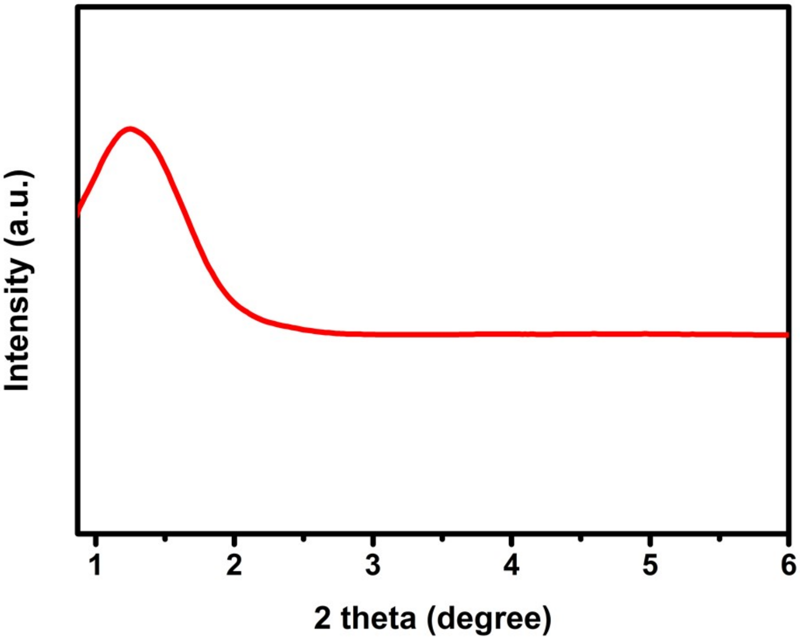

Fig. S5 Small-angle XRD pattern of the OMNiS-100 sample.

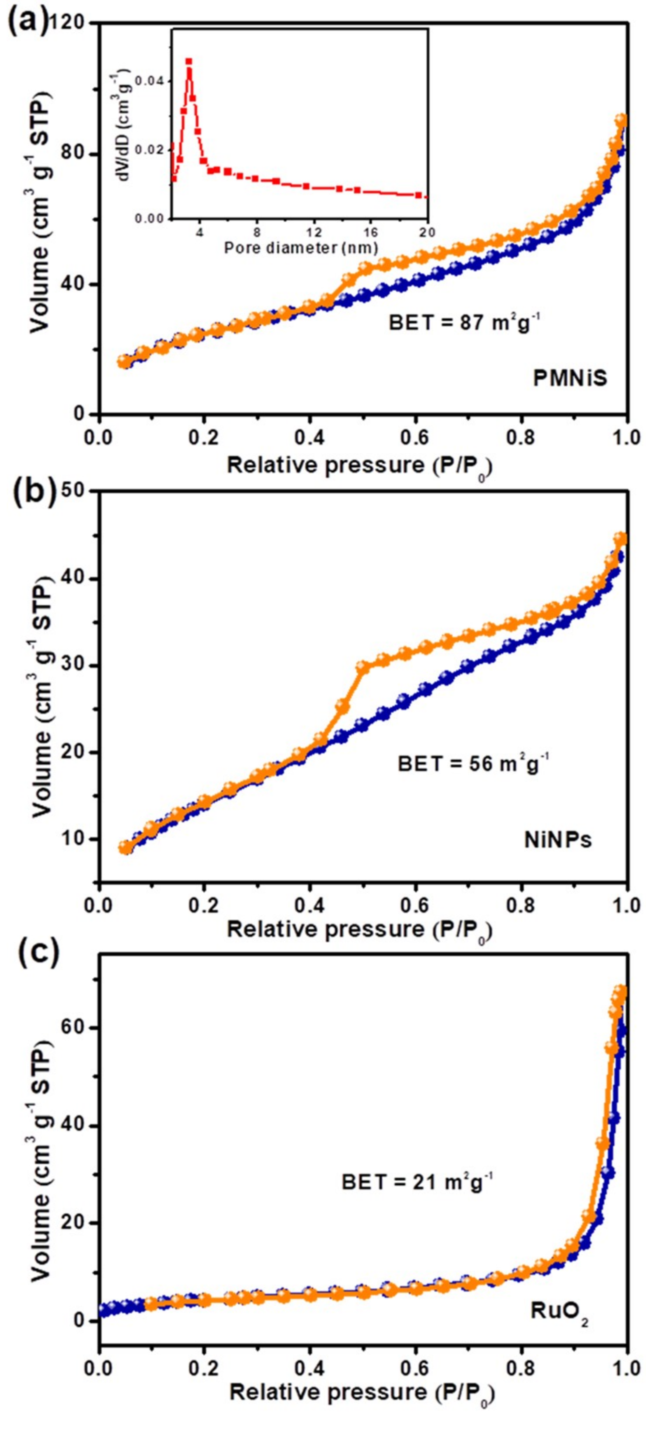

Fig. S6 (a) Nitrogen adsorption-desorption isotherms and pore size distribution curve (inset) for PMNiS. Nitrogen adsorption-desorption isotherms for NiNPs (b), and RuO_2 (c).

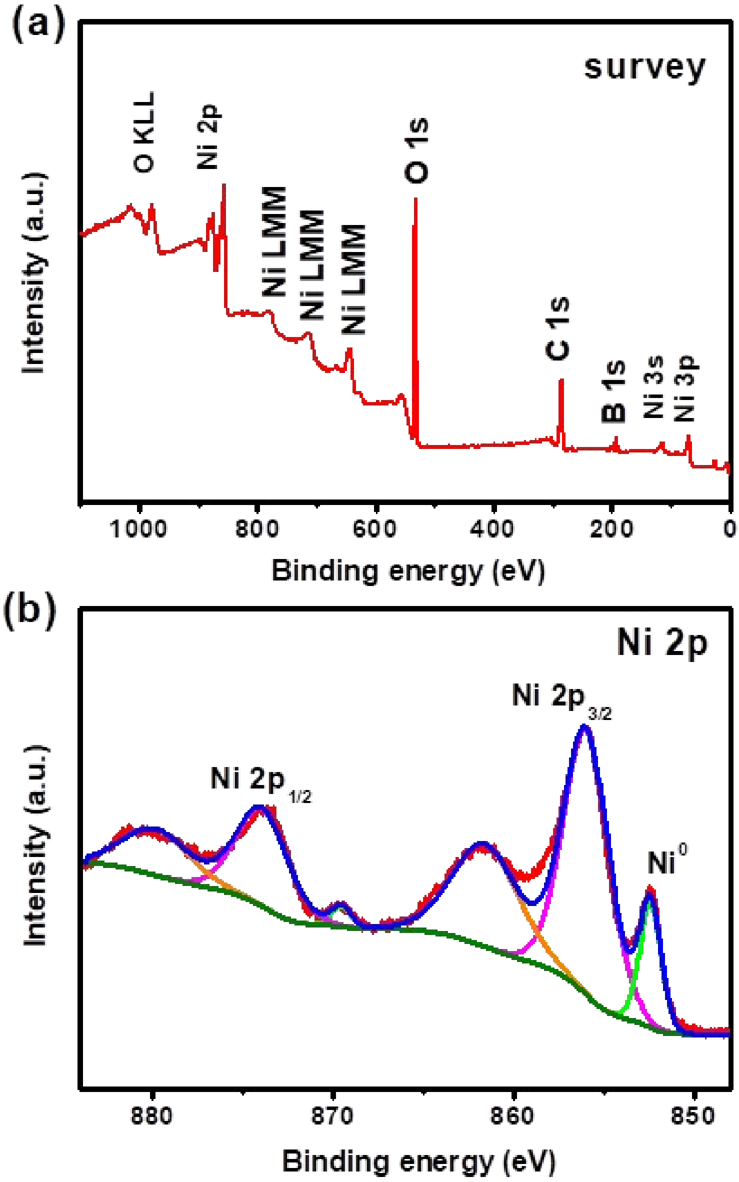

Fig. S7 (a) XPS survey spectrum of the OMNiS-100. (b) High resolution Ni 2p XPS spectrum of OMNiS-100.

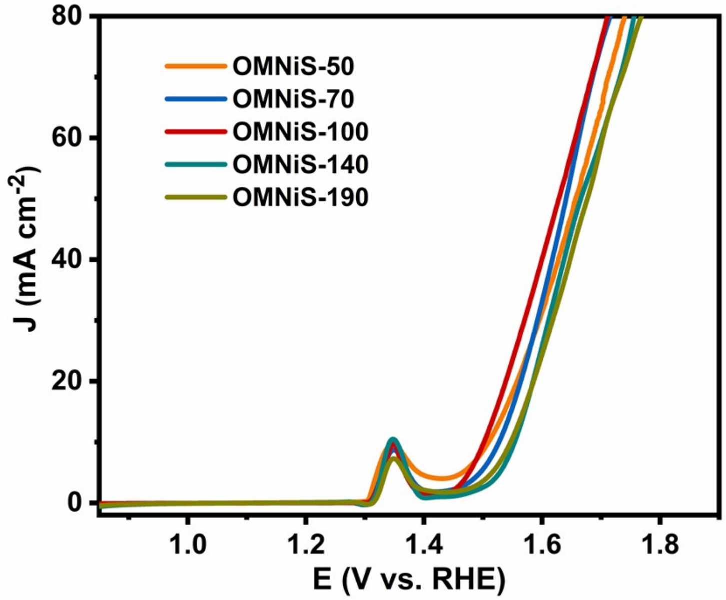

Fig. S8 OER LSV curves of different OMNiS samples in an O_2-saturated 0.1 M KOH electrolyte at a scan rate of 5 mV s^{-1}.

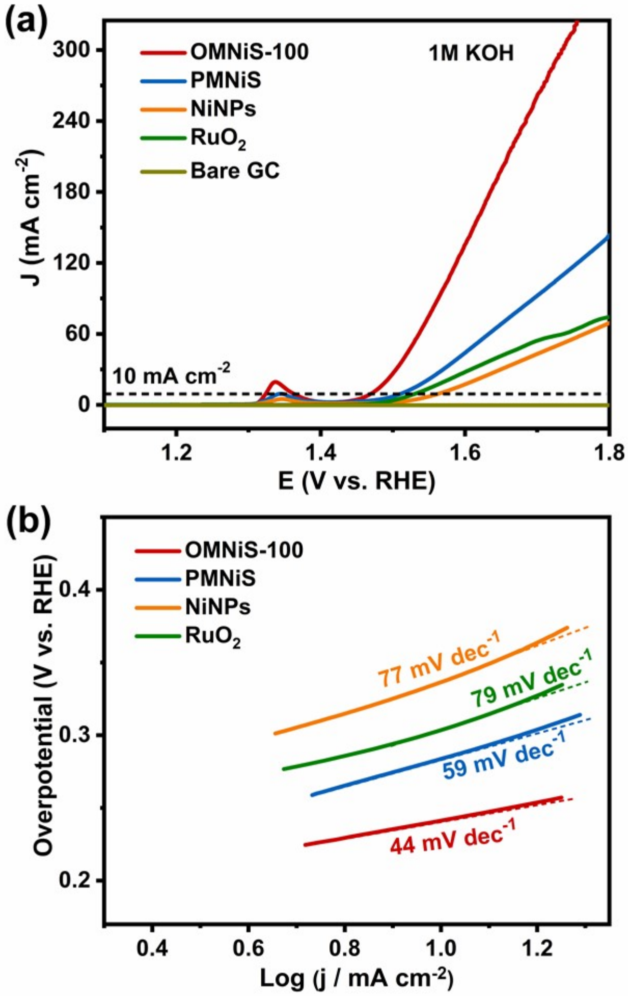

Fig. S9 (a) OER LSV curves of the OMNiS-100, PMNiS, NiNPs, and commercial RuO_2 catalysts, as well as a bare GC electrode in an O_2-saturated 1.0 M KOH electrolyte at a scan rate of 5 mV s^{-1}. (b) The corresponding Tafel plots derived from (a).

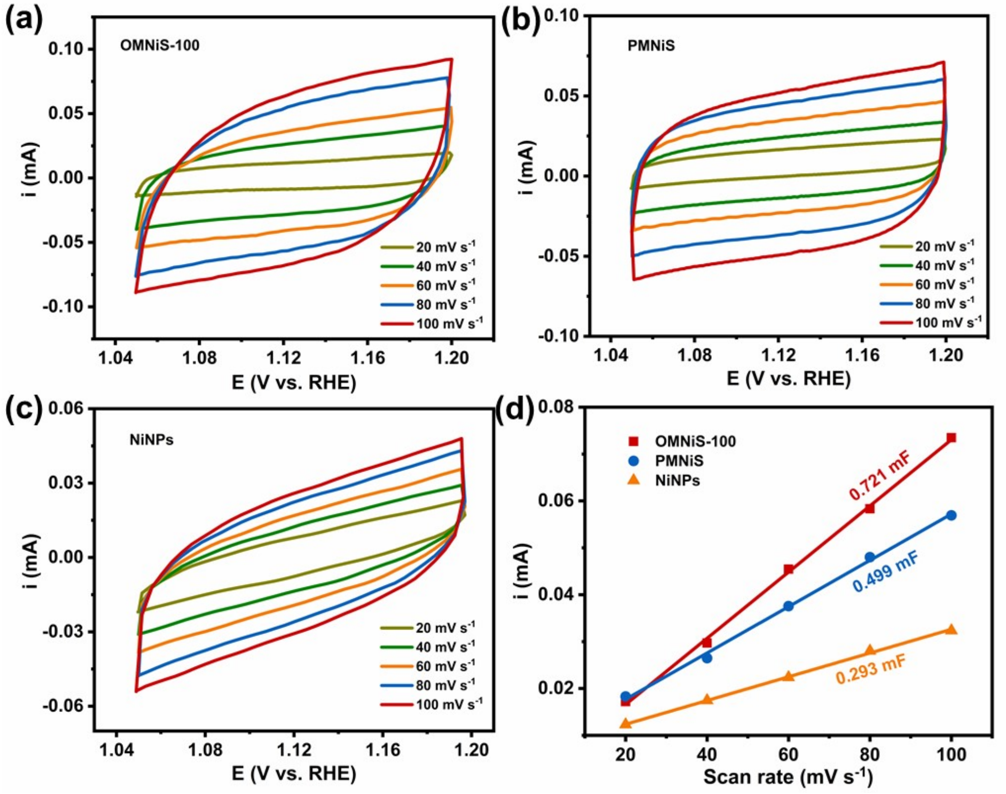

Fig. S10 CV curves of various samples in the region of 1.05~1.20 V vs. RHE (a) OMNiS-100, (b) PMNiS, and (c) NiNPs. The scan rates increase from 20 to 100 mV s^{-1}. (d) Plots of the current density at 1.15 V vs. the scan rates. The linear slope is the double layer capacitance (C_{DL}).

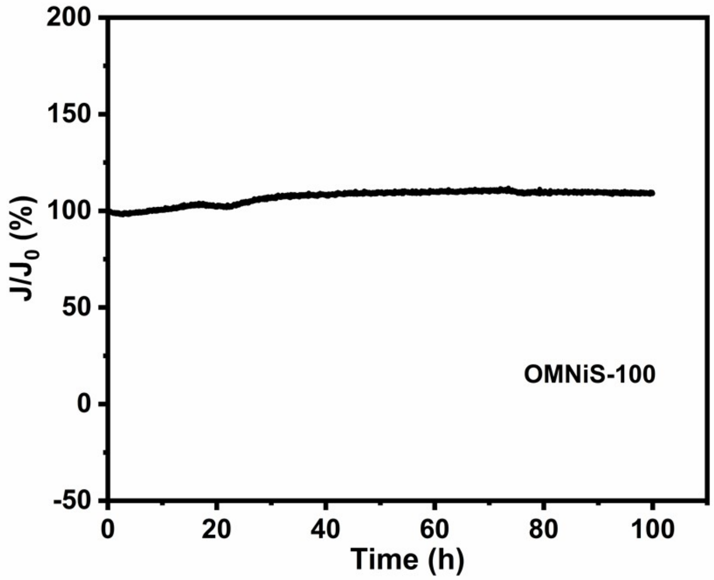

Fig. S11 Chronoamperometric responses of OMNiS-100 at 1.65 V vs. RHE for 100 h.

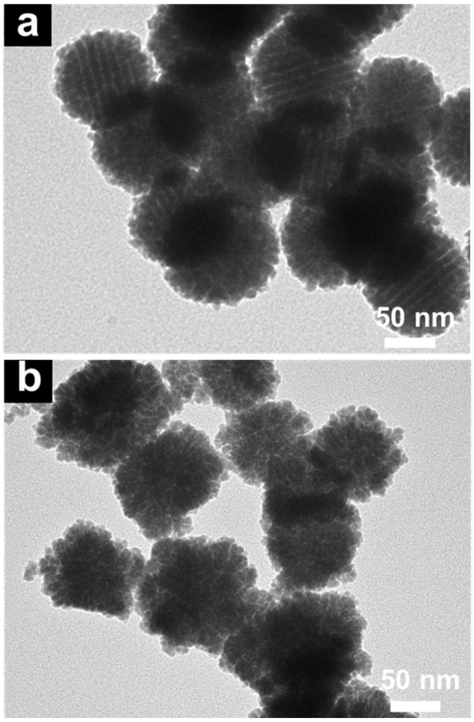

Fig. S12 The TEM images of OMNiS-100 (a) and NiNPs (b) after OER test.

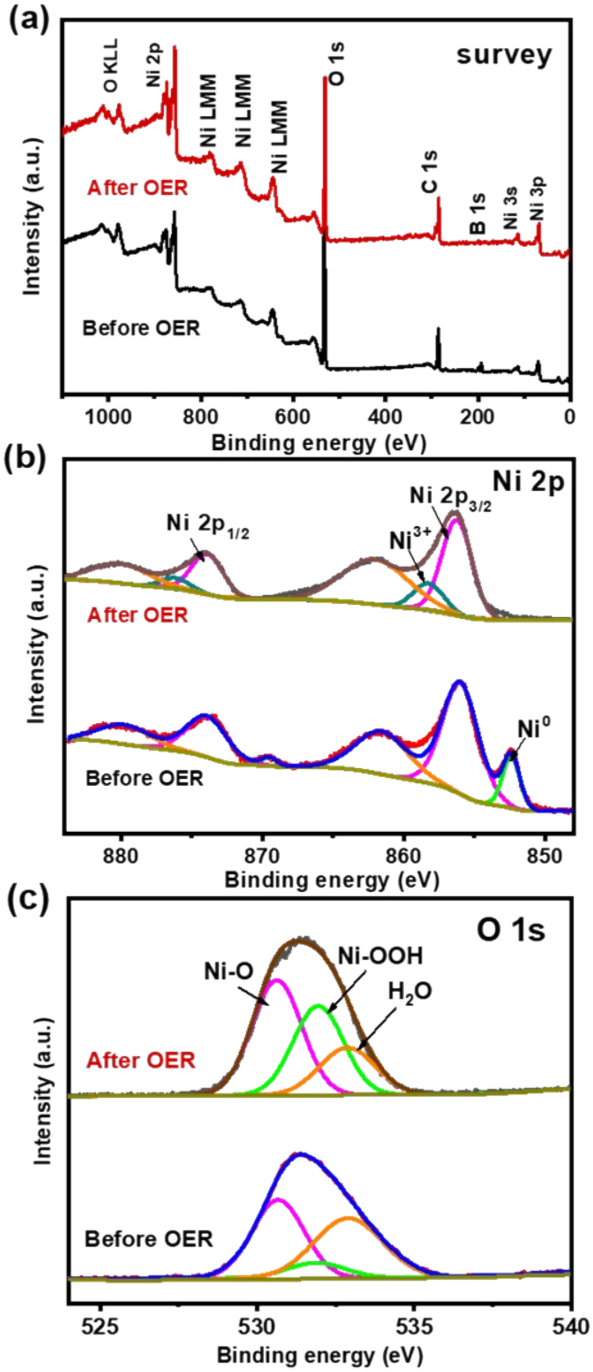

Fig. S13 XPS survey spectra (a), high resolution Ni 2p spectra (b) and high resolution O 1s spectra (c) of the OMNiS-100 catalyst before and after the OER tests.

3. Supplementary Tables

Table S1. Comparison of the electrocatalytic OER activity of OMNiS-100 with other recently reported Ni-based OER catalysts.

catalyst	electrolyte	overpotential at 10 mA cm^{-2} (mV vs. RHE)	Tafel slope (mV decade^{-1})	reference
OMNiS-100	**0.1 M KOH**	**271**	**56**	**This work**
p-$Cu_{1-x}NNi_{3-y}$/FeNiCu	1.0 M KOH	300	52	3
activated NiO_xH_y	1.0 M KOH	327	48	4
B-, P- and O-doped amorphous nickel nanoalloy	1.0 M KOH	370	90	5
CoS_2-$NiCo_2S_4$/N, S-codpoed graphene	1.0 M KOH	272	62.8	6
boronized Ni	1.0 M KOH	300	43	7
CuO-NiO/NF	1.0 M NaOH	319	86.4	8
oxygen-enriched NiFe-LDH	1.0 M KOH	310	74	9
Ni_2Si	0.1 M KOH	570	94	10
Ni_2P nanowire clusters	1.0 M KOH	280	46	11
Ni(Fe)OOH	1.0 M KOH	300	59	12

References

1. C. C. L. McCrory, S. Jung, J. C. Peters and T. F. Jaramillo, *J. Am. Chem. Soc.*, 2013, **135**, 16977-16987.
2. Y. Duan, Z. Yu, S. Hu, X. Zheng, C. Zhang, H. Ding, B. Hu, Q. Fu, Z. Yu, X. Zheng, J. Zhu, M. Gao and S. Yu, *Angew. Chem. Int. Ed.*, 2019, **58**, 15772-15777.
3. Y. Zhu, G. Chen, Y. Zhong, Y. Chen, N. Ma, W. Zhou and Z. Shao, *Nat. Commun.*, 2018, **9**, 2326.
4. J. Hu, D. Jiang, Z. Weng, Y. Pan, Z. Li, H. Du and Y. Yuan, *Chem. Eng. J.*, 2022, **430**, 132736.
5. X. Liu, J. Wu and X. Guo, *Electrochem. Commun.*, 2020, **111**, 106649.
6. R. Zhang, S. Cheng, N. Li and W. Ke, *Appl. Surf. Sci.*, 2020, **503**, 144146.
7. J. Li, H. Chen, Y. Liu, R. Gao and X. Zou, *J. Mater. Chem. A*, 2019, **7**, 5288-5294.
8. C. Li, B. Zhang, Y. Li, S. Hao, X. Cao, G. Yang, J. Wu and Y. Huang, *Appl. Catal. B: Environ.*, 2019, **244**, 56-62.
9. H. Chen, Q. Zhao, L. Gao, J. Ran and Y. Hou, *ACS Sustain. Chem. Eng.*, 2019, **7**, 4247-4254.
10. R. Kumar, M. Bahri, Y. Song, F. Gonell, C. Thomas, O. Ersen, C. Sanchez, C. Laberty-Robert and D. Portehault, *Nanoscale*, 2020, **12**, 15209-15213.
11. D. Xiang, B. Zhang, H. Zhang and L. Shen, *Front. Chem.*, 2021, **9**, 773018.
12. H. Yang, L. Gong, H. Wang, C. Dong, J. Wang, K. Qi, H. Liu, X. Guo and B. Y. Xia, *Nat. Commun.*, 2020, **11**, 5075.